Supplementary Materials

Do Grain Boundaries Dominate Non-Radiative Recombination in $CH_3NH_3PbI_3$ Perovskite Thin Films?

Mengjin Yang,[a] Yining Zeng,[b*] Zhen Li,[a] Dong Hoe Kim,[a] Chun-Sheng Jiang,[c] Jao van de Lagemaat[a*] and Kai Zhu[a*]

[a] Chemistry and Nanoscience Center, National Renewable Energy Laboratory, 15013 Denver West Parkway, Golden, CO 80401 (USA)

[b] Biosciences Center, National Renewable Energy Laboratory, 15013 Denver West Parkway, Golden, CO 80401 (USA)

[c] Material Science Center, National Renewable Energy Laboratory, 15013 Denver West Parkway, Golden, CO 80401 (USA)

[*]Corresponding authors: Yining.Zeng@nrel.gov (YZ); Jao.vandeLagemaat@nrel.gov (JvdL); Kai.Zhu@nrel.gov (KZ)

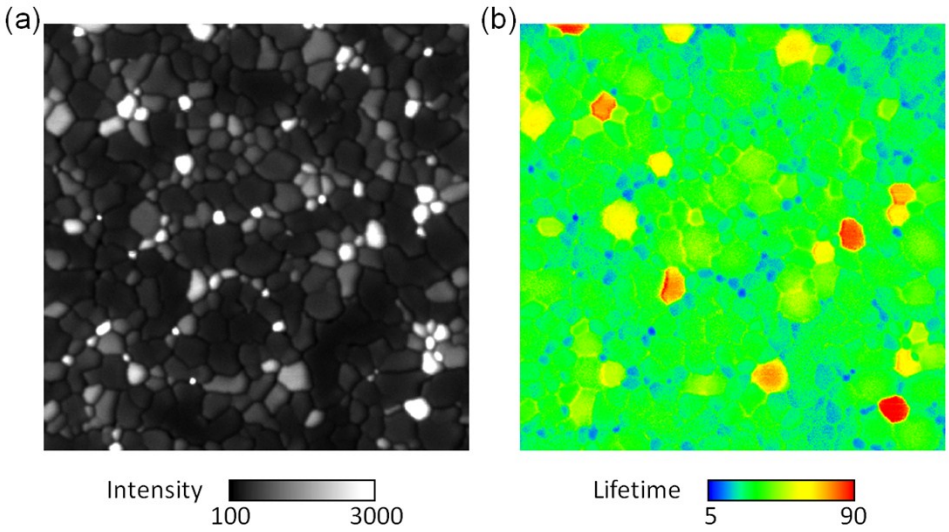

Figure S1. FLIM imaging result. Respective images of (**a**) Intensity and (**b**) lifetime of Figure 1a.

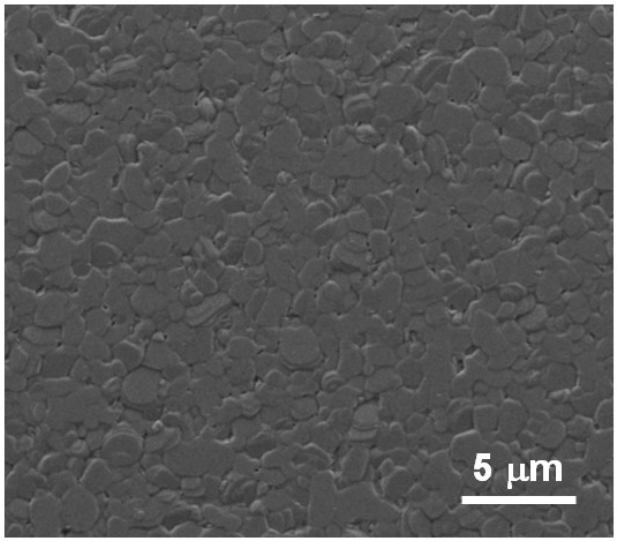

Figure S2. Top view of the SEM image of the perovskite $MAPbI_3$ films used in FLIM study.

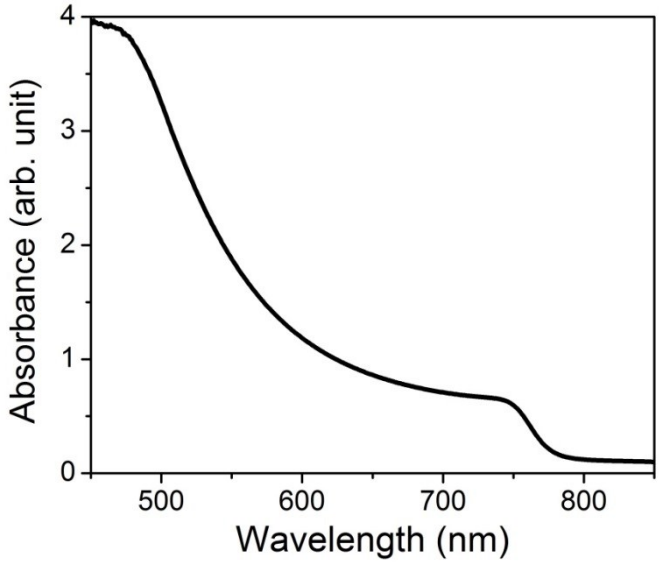

Figure S3. UV-vis absorption spectrum of the perovskite $MAPbI_3$ films used in FLIM study.

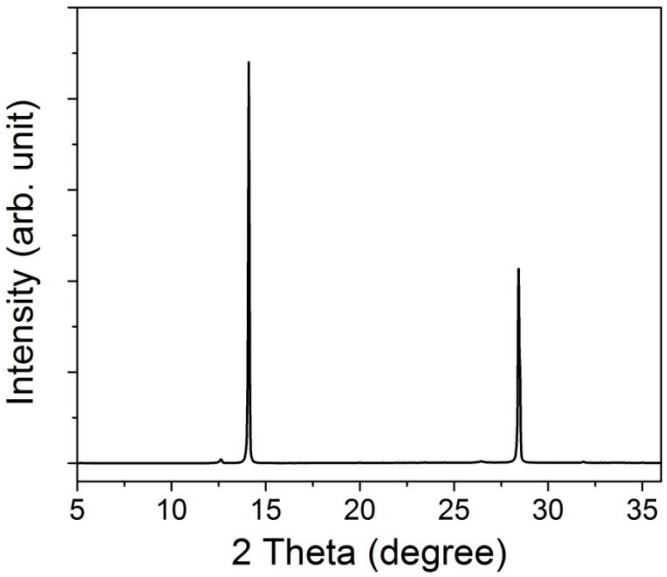

Figure S4. X-ray diffraction pattern of the perovskite $MAPbI_3$ films used in FLIM study.

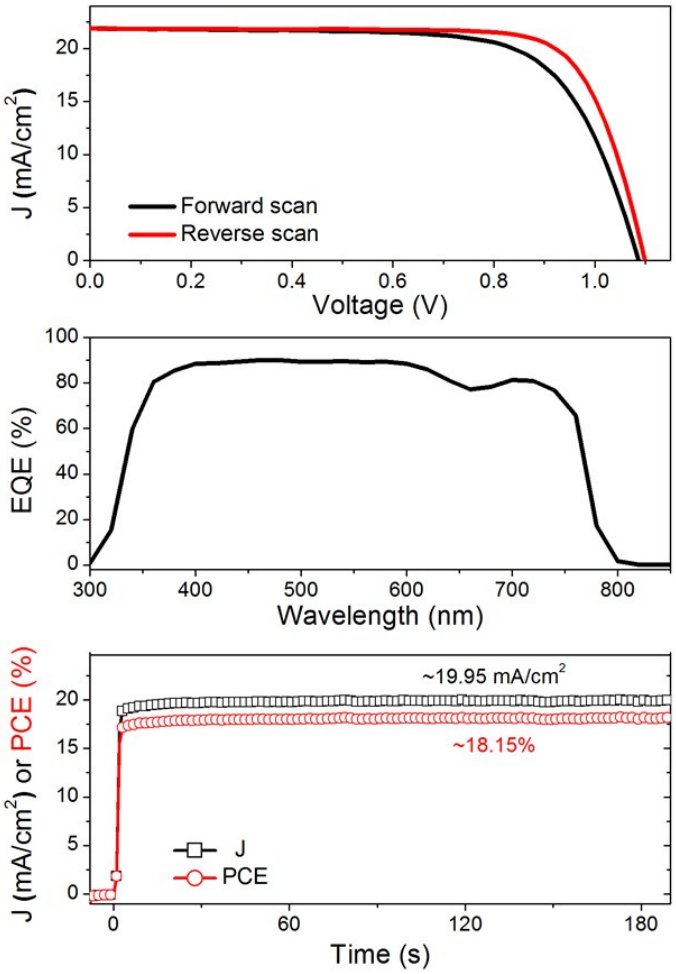

Figure S5. Device characteristics based on the perovskite $MAPbI_3$ films used in FLIM study. (**a**) Plots of current density-voltage (*J–V*) curves under reverse and forward voltage scans. For the reverse scan, the device shows the power conversion efficiency (PCE) of 18.52%, with short-circuit current density (J_{sc}) of 21.88 mA/cm^2, open-circuit voltage (V_{oc}) of 1.099 V, and fill factor (FF) of 0.770. For the forward scan, the device shows a PCE of 16.82%, with J_{sc} of 21.94 mA/cm^2, V_{oc} of 1.086 V, and FF of 0.706. (**b**) External quantum efficiency (EQE) spectra, which has an integrated photocurrent density of about 21.31 mA/cm^2. (**c**) Stabilized photocurrent density (~19.95 mA/cm^2) and power conversion efficiency (~18.15%) biased near the maximum power point were observed for several minutes under continuous light soaking.

Supplementary Note 1: Surface potential and topography analysis.

We measured the surface-potential distribution of the perovskite films using KPFM.[1, 2] Figure S6a shows a typical KPFM image over a 5×5 μm^2 area. In comparison to the neighboring grains, GBs show higher (more positive) surface potential, suggesting a downward band-bending around the GBs in the likely lightly doped p-type material.[3] Figures S6b,c show two typical line-scans of surface-potential distribution across several consecutive grains as indicated in Figure S6a. Both line-scans show that the potentials at the GBs are about 100 mV higher than those from the adjacent grain surfaces, whereas the potentials along the grain surfaces are relatively unchanged. Figure S6d–f shows the corresponding topography and line profile analysis; there is no significant cross-talk between topography and potential images. The magnitude of surface potential bending is similar to that measured for CIGS, CZTS, and CdTe (~100–300 mV).[4, 5] However, because of the likelihood of surface depletion-induced potential gradient from the bulk toward the surface, it is difficult to determine the absolute value of band bending at GBs inside the film from the surface-potential mapping. Nevertheless, the positive potential peak is expected to attract electrons (minority carriers) into GBs and repel photogenerated holes away from GBs. Although this positive potential at the GBs could facilitate a conducting channel along GBs,[6, 7] it could also presents a potential barrier that inhibits carriers from moving freely across the GBs. This could explain why we see sharp transitions of FLIM results across two adjacent grains (Figure 1).

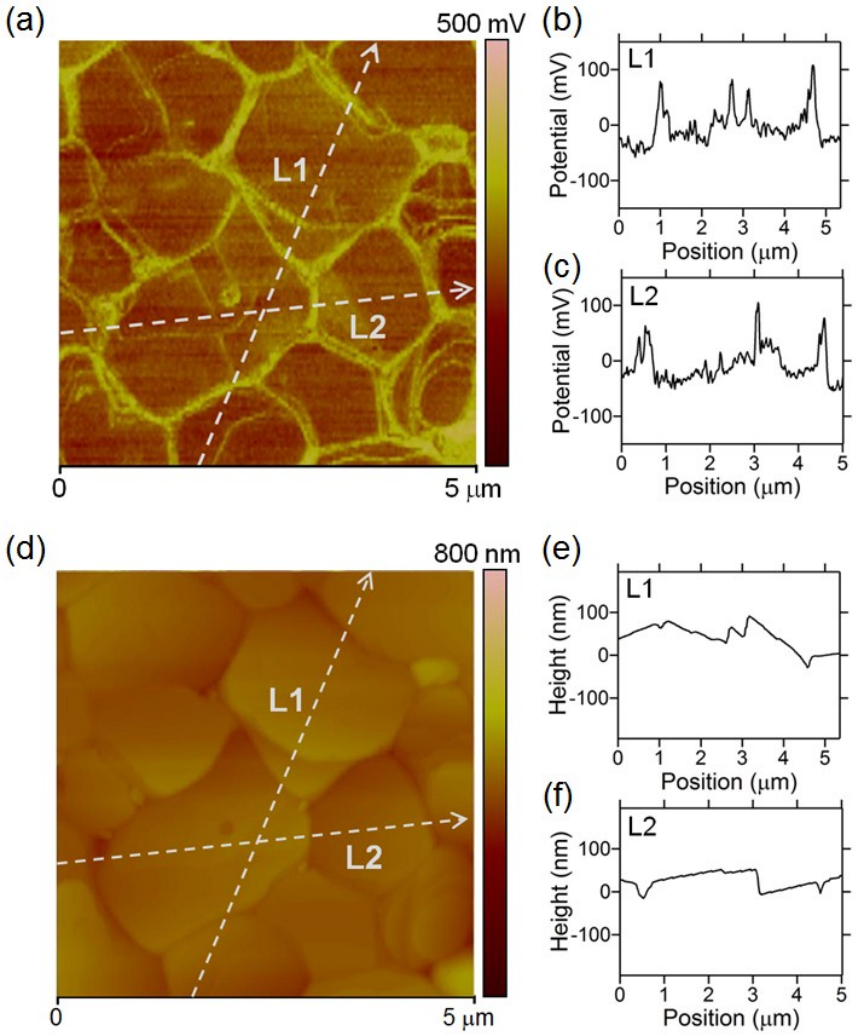

Figure S6. Surface potential mapping and topography image and line-profile analysis. (**a**) Typical KPFM surface potential image taken on a perovskite film. (**b, c**) Two typical line scans (as indicated in (a)) of potential profiles indicating about 100 mV more positive potential at grain boundary relative to the grain interior. (**d**) Topography image taken together with the potential image shown in (a). (**e, f**) Two typical line profiles as indicated in (a and d).

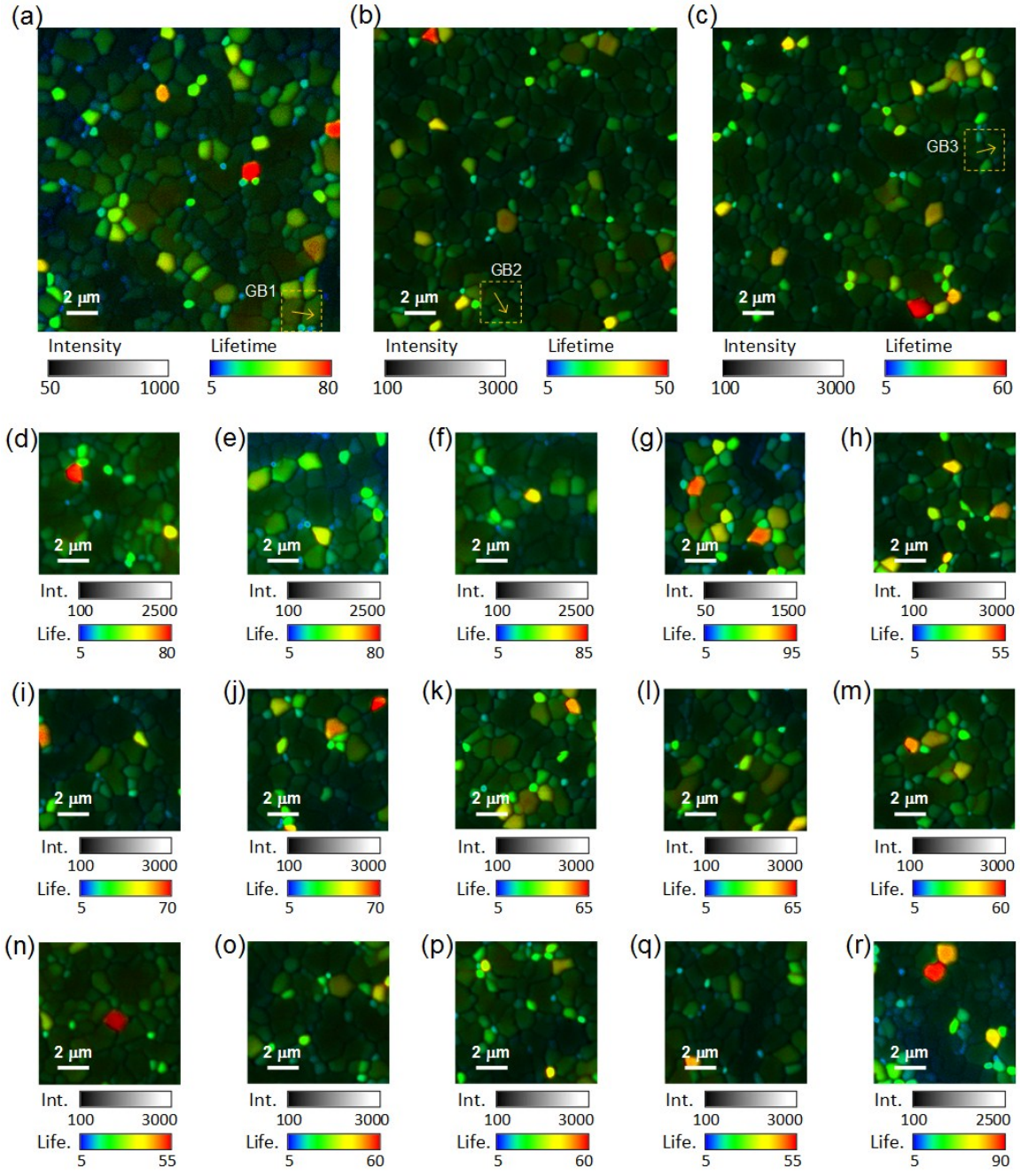

Figure S7. Typical FLIM images from multiple samples. (**a**)–(**r**) represent measurements from samples prepared over about 6-month time period.

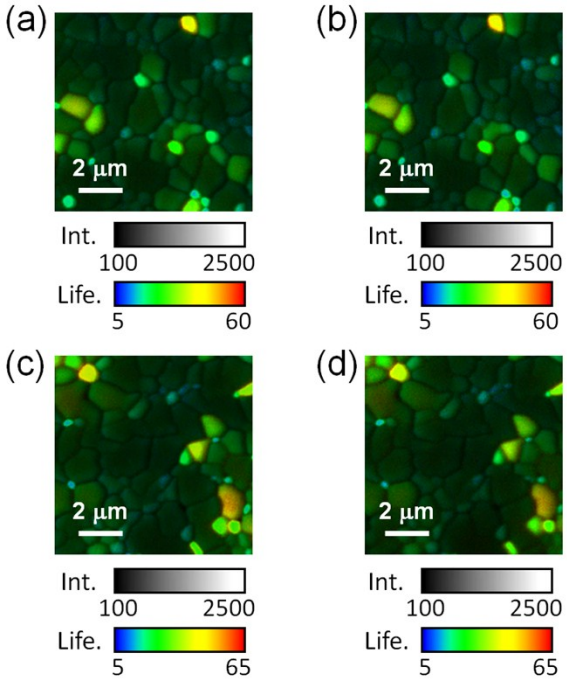

Figure S8. Stability of perovskite films under FLIM measurement. (**a**) and (**c**) represent FLIM measurement immediately after the samples were prepared. (**b**) and (**d**) represent FLIM measurement on the same samples shown in (**a**) and (**c**) after 4–8 hours in the ambient condition.

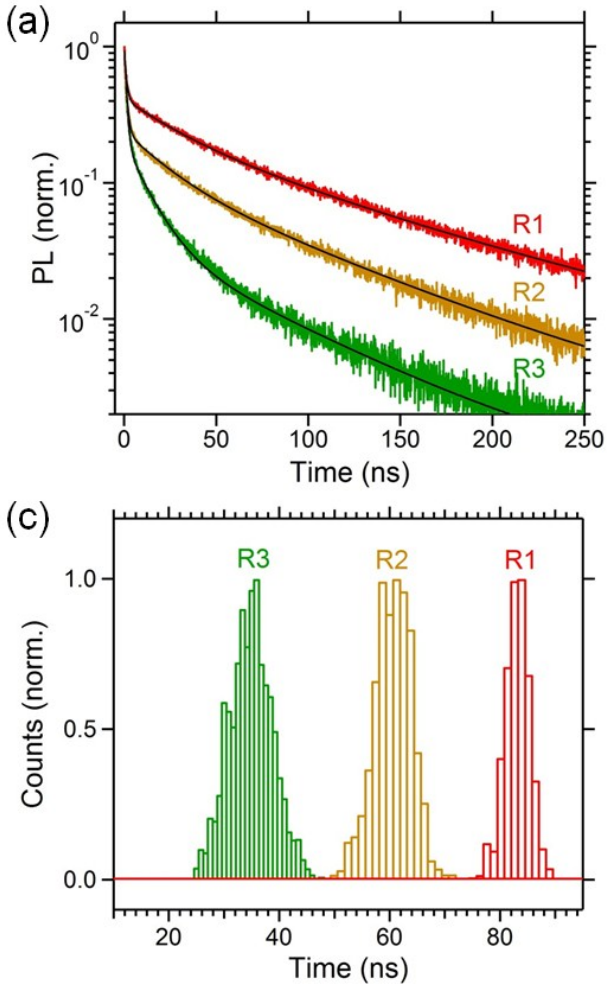

Figure S9. FLIM lifetime. (**a**) Time-correlated single-photon counting traces (TCSPC; corresponding to time-resolved PL decay) for three typical grains indicated in the FLIM image (R1–3 in Fig. 1a). The color of the three traces approximates the lifetime color in the FLIM image. The black lines are the best fits to a three-exponential decay model, from which an intensity-weighted average lifetime can be derived (R1: 83.7 ns; R2: 61.3 ns; R3: 34.1 ns). (**b**) Histograms of FLIM lifetime distribution for the three grains shown in (a). The average lifetime from a three-exponential fitting shown in (a) matches well with the peak distribution of FLIM lifetimes; thus, it represents a good and convenient mathematical description of the FLIM decay kinetics that allows for easy analysis for individual grains.

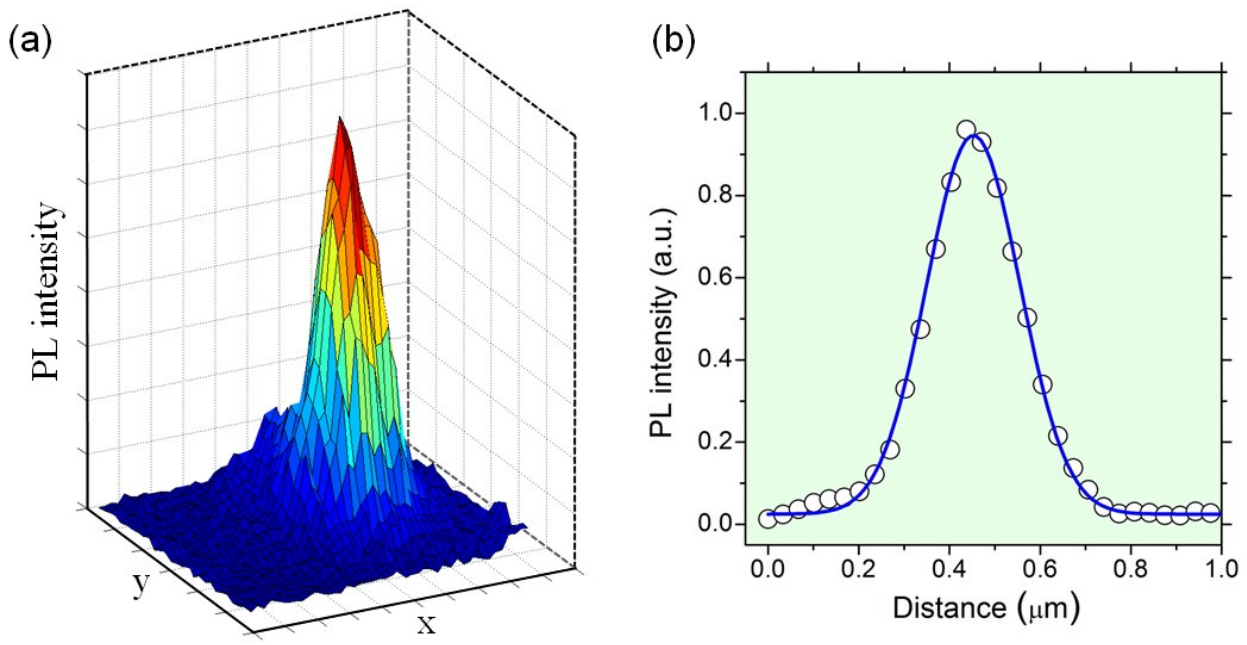

Figure S10. FLIM point-spread function (PSF) determination. (a) 3D plot of fluorescence spot of a 100 nm microsphere obtained by the FLIM setup. **(b)** Typical PL line scan across the fluorescence microspheres to determine the PSF. Circle: experimental data; blue line: Gauss fitting showing σ_0=103 nm; FWHM=242 nm. Within the resolution limit, sharp changes in FLIM intensities and lifetimes across grain boundaries are clearly visible as shown in Figure 1b.

Supplementary Note 2: Fitting method explanation

Immediately after excitation and before the carriers have reached a grain boundary, the excess electron and hole density follows assuming no recombination and in two dimensions.[8]

$$n(x,y,t) = \frac{N_0}{\pi(8Dt + 2\sigma_0^2)} exp\left(\frac{x^2 + y^2}{8Dt + 2\sigma_0^2}\right) \quad \text{(S1)}$$

in which, D is the average diffusion coefficient of electrons and holes, N_0 is the initial number of carriers integrated over the pulse and σ_0 is the standard deviation of the beam profile, which is related to the full-width at half max (W) by $W = 2\sqrt{2ln2}\sigma_0 \approx 2.355\,\sigma_0$. For our setup σ_0 was determined to be about 100 nm (Figure S10). The PL intensity as a function of time is defined by the convolution of $n(x,y,t)$ with the beam profile (Equation S1 omitting the prefactor and at t = 0). This convolution and accounting for carrier recombination using a simple exponential decay with lifetime τ_{PL}, yields for the PL intensity as a function of time normalized to 1 at t = 0:

$$I_{PL} = \frac{\sigma_0^2}{2Dt + \sigma_0^2} exp\left(-\frac{t}{\tau_{PL}}\right) \quad \text{(S2)}$$

Figure S11 shows the PL decay traces on a double-exponential scale for grains with relatively large grain sizes (as indicated). It is worth to note that the instrument response time of the FLIM setup is about 0.25 ns and the time step used in the FLIM measurement is 0.128 ns. It is clear that the Equation S2 fits the results well for these grains. The residuals for each of these fits are also shown and indicate that the fitting quality is good. From these fits, we estimate the diffusion coefficient is about 0.095±0.010 cm^2s^{-1}. In contrast, the fits do not work well for small grains as illustrated in Figure S12 (grain size 1.3 and 0.5 μm^2) and yield an unphysically low carrier diffusion coefficient because they do not account for the fact that the grain boundaries are impervious to carriers.

We also implemented a fully 3D model in COMSOL multiphysics that considers diffusion of charge carriers, bulk, surface, and grain boundary recombination (or transfer to the next grain), and photon recycling using the below coupled equations in the bulk of the grain:[9]

$$\frac{dn}{dt} = G + D\nabla^2 n - An^3 - Bn^2 - C^{'}n + \frac{c}{n_s}\sum_{\lambda}\alpha_\lambda \gamma_\lambda \quad \text{(S3)}$$

$$\frac{d\gamma_\lambda}{dt} = \left(Bn^2 P_{stay}\right)P_\lambda + D_\lambda \nabla^2 \gamma_\lambda - \frac{c}{n_s}\alpha_\lambda \gamma_\lambda \quad \text{(S4)}$$

in which $C^{'}$ is the monomolecular recombination rate constant only considering bulk recombination, n_s is the refractive index of the perovskite layer, c is the speed of light, γ_λ is the density of photons of wavelength λ in the perovskite, P_{stay} is the probability that an emitted photon will be guided inside the film by total internal reflection, and P_λ is the probability that light is emitted at wavelength λ. G is described by a Gaussian pulse in time and space with a temporal width (standard deviation) of 100 ps and a spatial width of 103 nm (see Figure S10). The absorption coefficient in the perovskite at the excitation wavelength of 405 nm was taken to be 14×10^4 cm^{-1}. We approximate the sum over wavelengths in Equations S3 and S4 by assuming that the perovskite emits only at one wavelength λ_{max} with a $P_\lambda = 1$. For the purposes of this calculation this does not have a discernable influence on the outcomes as we are not interested in the actual spectrum of the emission. For the purposes of the simulation, we describe top and surface recombination as a flux of carriers out of the simulation volume of magnitude R_s*n and grain boundary recombination as a flux R_{gb}*n. For the photon density, the grain boundaries are transparent, but the top and bottom surfaces are not. Also, the parameter D_λ is given by $D_\lambda = \frac{c}{n_s \alpha}\frac{1}{}$, which is about 40 m^2/s. The Equation S4 is valid in the situation where light is scattered inside the layer. It would be more appropriate in the thin film limit to do a full optical modeling using Maxwell's equations, but we consider that outside the scope of the current paper and for the purposes of the current paper this approximation is sufficient. Figure S13 shows the temporal behavior of the carrier density n as a function of time for a square 1×1 μm grain where the laser beam is incident just to the side of the middle. It is clear from Figure S13 that the carrier density is basically equilibrated after about 5 ns even for a 1 μm^2 grain. When we turn off photon recycling in this calculation by setting P_{stay} to zero, there is no visible difference.

The effect of photon recycling on the dynamics of carriers is further illustrated by the calculated FLIM transients (Figure S14) for the same grain shown in Figure S13.

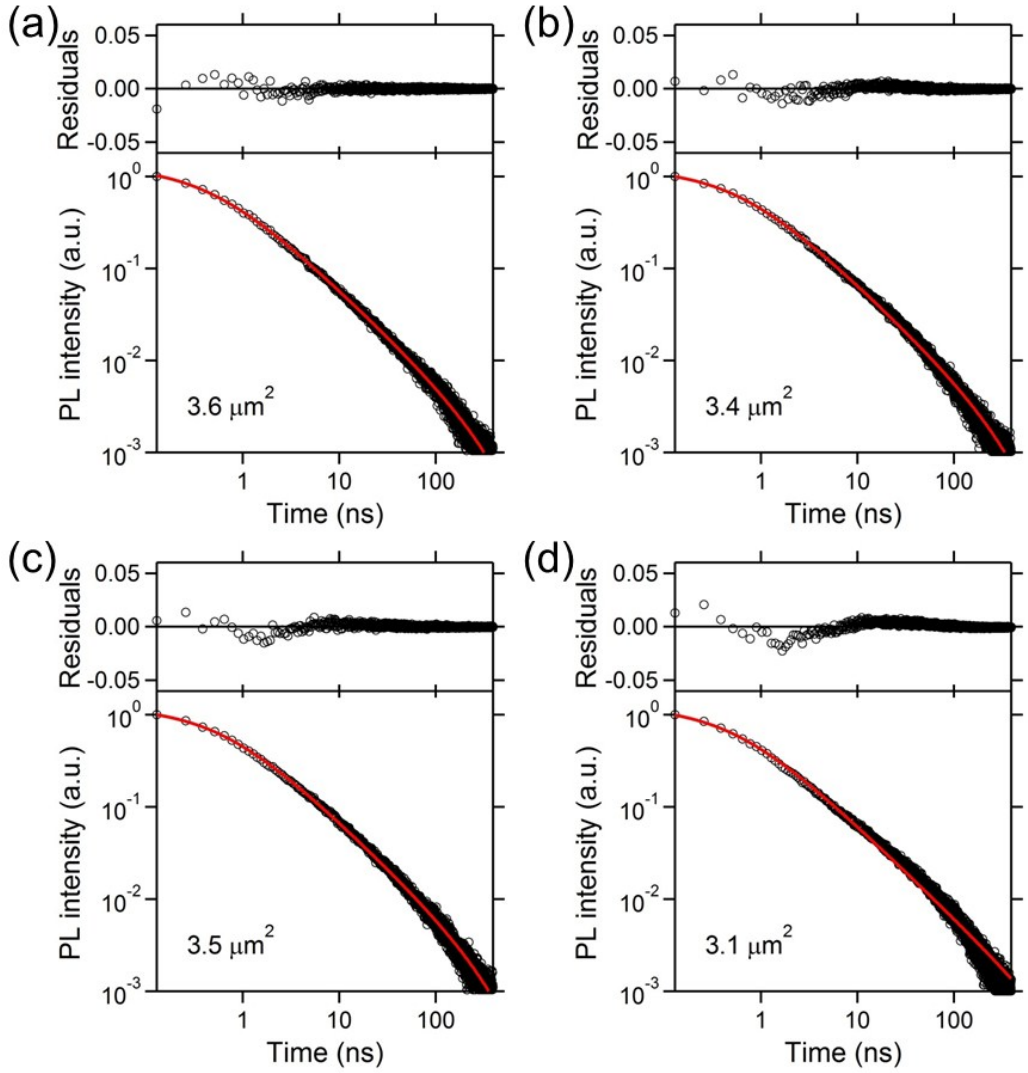

Figure S11. Typical PL decay traces for large grains. (**a**)–(**d**) correspond to four different grains (grain size indicated). The red lines are the fits. The residuals are also shown for each of these fits.

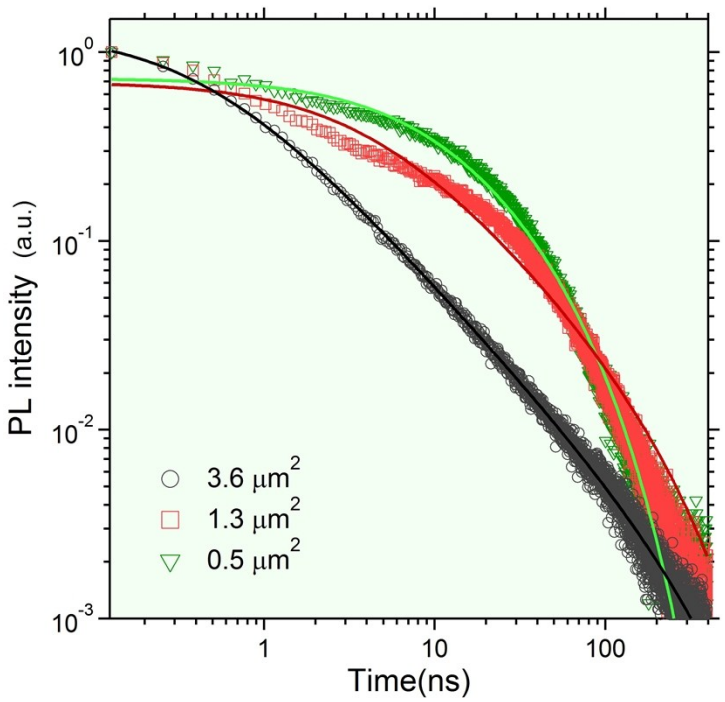

Figure S12. PL decay traces for three typical grains of different grain areas as indicated. The continuous lines are fits to Equation S2.

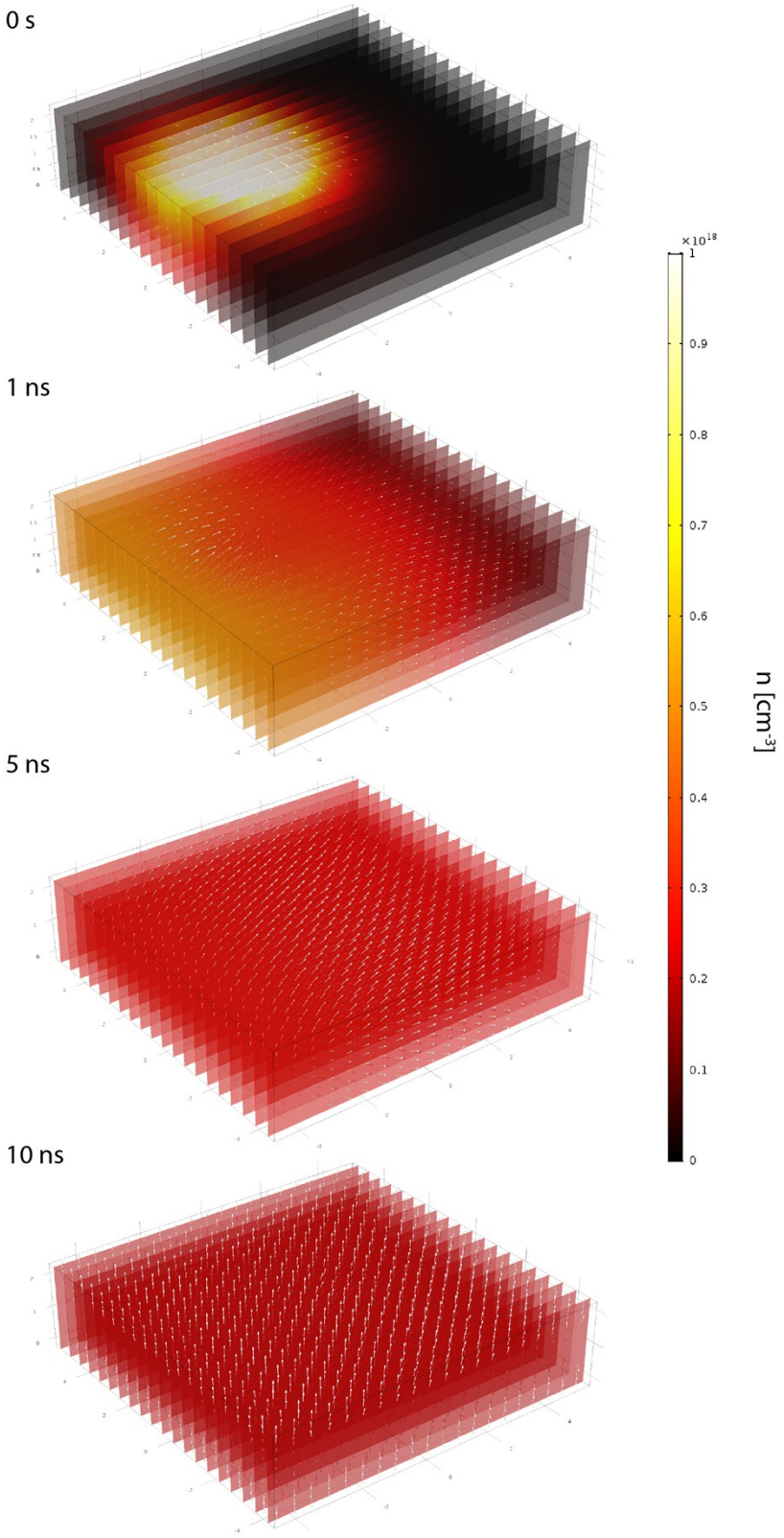

Figure S13. Time dependence of the electron concentration after excitation at t=0 (peak of the light pulse). The white arrows show the flux lines of the carriers.

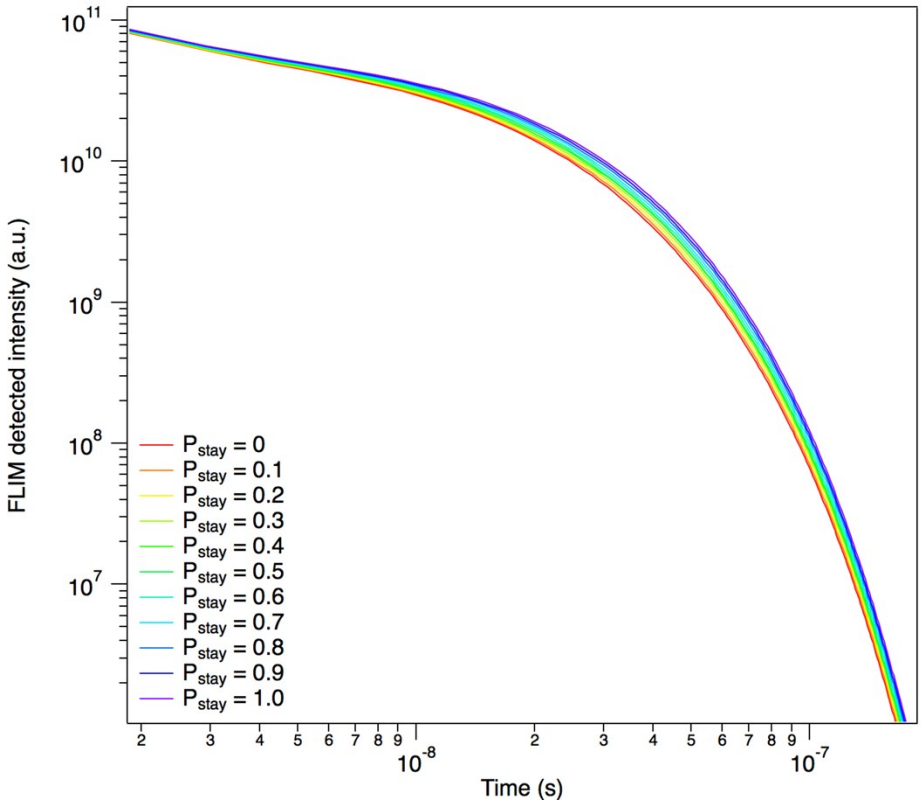

Figure S14. FLIM transients calculated by integrating B^*n^2 over the confocal detection volume in the COMSOL simulation (a Gaussian detection efficiency centered at the confocal spot) as a function of the probability that photons are emitted into the perovskite layer. The FLIM lifetime is not strongly influenced and there only is a minor increase in the intensity of the detected luminescence.

Supplementary Note 3: Stochastic modeling of the influence of a distribution in grain sizes and film thickness on the FLIM lifetime.

The variation in in FLIM lifetime observed in the main text can be explained by simple statistical variations between grains. The grain size shows a lognormal distribution in size (Figure S15).We expect the same to be true for the film thickness (see also Figure S6).

Assuming the above log-normal distribution of grain sizes (Figure S15) and a log-normal distribution of film thicknesses with an average thickness of 250 nm and a half width spread of 100 nm, we can use Equations 3 and 5 in the main text to calculate a distribution of expected observations on the FLIM lifetime. In this calculation shown in Figure S16, we assume that film thickness and grain size are not correlated. It is clear from this figure that the experimentally observed spread in values can be accounted for by the variations in grain size and film thickness.

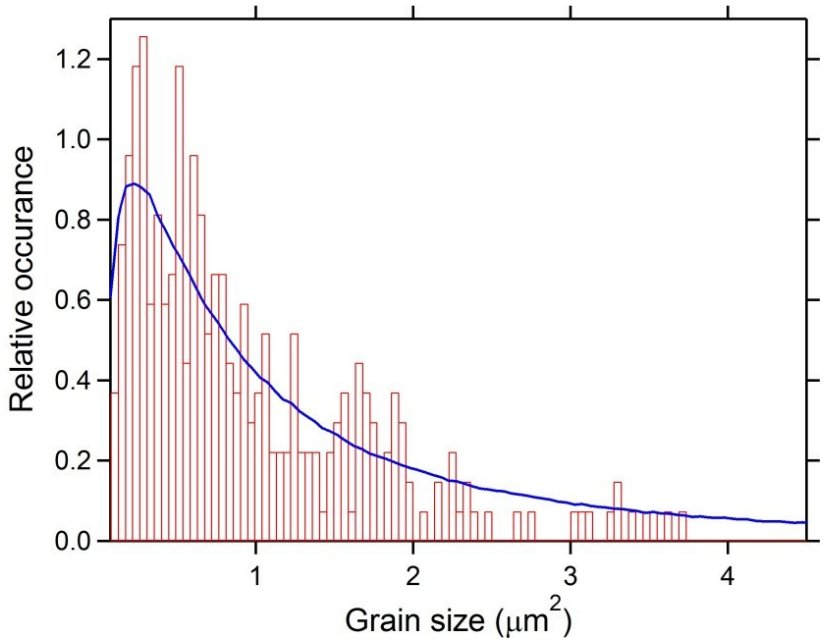

Figure S15. Relative distribution of the grain size. The continuous solid line shows a fit to a lognormal distribution.

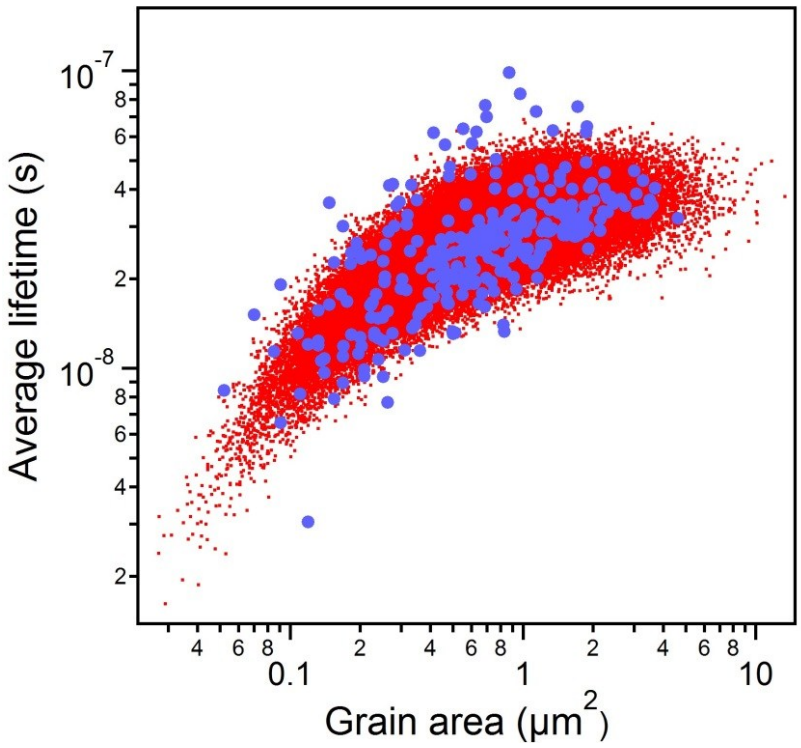

Figure S16. Dependence of the FLIM lifetime on grain size. Experimental data in blue, red points are the result of a simple Monte Carlo model with lognormal distributions of grain size and film thickness. The values for R_s and R_{gb} are the same as quoted in the main text.

References

1. M. Nonnenmacher, O'Boyle M. P., Wickramasinghe H. K. Kelvin probe force microscopy. *Appl. Phys. Lett.* **58**, 2921-2923 (1991).
2. A. Kikukawa, Hosaka S., Imura R. Silicon pn junction imaging and characterizations using sensitivity enhanced kelvin probe force microscopy. *Appl. Phys. Lett.* **66**, 3510-3512 (1995).
3. C. S. Jiang*, et al.* Carrier separation and transport in perovskite solar cells studied by nanometre-scale profiling of electrical potential. *Nat. Commun.* **6**, 8397 (2015).
4. C.-S. Jiang*, et al.* Local built-in potential on grain boundary of cu(in,ga)se2 thin films. *Appl. Phys. Lett.* **84**, 3477-3479 (2004).
5. J. B. Li, Chawla V., Clemens B. M. Investigating the role of grain boundaries in czts and cztsse thin film solar cells with scanning probe microscopy. *Adv. Mater.* **24**, 720-723 (2012).
6. J. S. Yun*, et al.* Benefit of grain boundaries in organic-inorganic halide planar perovskite solar cells. *J. Phys. Chem. Lett.* **6**, 875-880 (2015).
7. G. Y. Kim*, et al.* Efficient carrier separation and intriguing switching of bound charges in inorganic-organic lead halide solar cells. *J. Phys. Chem. Lett.* **6**, 2355-2362 (2015).
8. Z. Guo, Manser J. S., Wan Y., Kamat P. V., Huang L. Spatial and temporal imaging of long-range charge transport in perovskite thin films by ultrafast microscopy. *Nat Commun* **6**, 7471 (2015).
9. L. M. Pazos-Outón*, et al.* Photon recycling in lead iodide perovskite solar cells. *Science* **351**, 1430-1433 (2016).